

## Article

# Low-Temperature-Aged Synthesis of CeO<sub>2</sub>-Coated Li-Rich Oxide as Cathode for Low-Cost High-Energy Density Li-Ion Batteries

Yanlin Liu <sup>1,3,4</sup> , Bin Li <sup>2</sup>, Min Chen <sup>2,3</sup> and Weishan Li <sup>2,3,\*</sup>

- <sup>1</sup> School of Automobile and Transportation Engineering, Guangdong Polytechnic Normal University, Guangzhou 510450, China; liuyanlin@gpnu.edu.cn
- <sup>2</sup> School of Chemistry, South China Normal University, Guangzhou 510006, China; lib120@163.com (B.L.); chenmin@m.scnu.edu.cn (M.C.)
- <sup>3</sup> National and Local Joint Engineering Research Center of MPTES in High Energy and Safety LIBs, Engineering Research Center of MTEES (Ministry of Education), Key Laboratory of ETESPG (GHEI), South China Normal University, Guangzhou 510006, China
- <sup>4</sup> School of Material and Energy, Guangdong University of Technology, Guangzhou 510006, China
- \* Correspondence: liwsh@scnu.edu.cn; Tel.: +86-02039310256

**Abstract:** Co-free Li-rich oxide shows promise as a cathode for low-cost high-energy density Li-ion batteries but presents poor cyclic stability. To address this issue, a novel CeO<sub>2</sub>-coated Li-rich oxide composite is developed by applying a layer of CeO<sub>2</sub> onto Co-free Li-rich oxide through a low-temperature-aged process. With this uniform coating, the resulting composite presents improved cyclic stability as well as rate capability as the cathode of a Li-ion battery. The capacity retention of the resulting composite is increased from 67% to 85% after 100 cycles, and its capacity retention of 5 C/0.05 C is enhanced from 10% to 23% compared with the uncoated sample. Such significant improvements indicate that this low-temperature-aged process is promising for preparing Co-free Li-rich oxides as cathodes of low-cost high-energy density Li-ion batteries.

**Keywords:** Li-rich oxide; surface coating; cerium oxide; low temperature aging; Li-ion battery



**Citation:** Liu, Y.; Li, B.; Chen, M.; Li, W. Low-Temperature-Aged Synthesis of CeO<sub>2</sub>-Coated Li-Rich Oxide as Cathode for Low-Cost High-Energy Density Li-Ion Batteries. *Batteries* **2023**, *9*, 330. <https://doi.org/10.3390/batteries9060330>

Academic Editors: Claudio Gerbaldi, Zhuosen Wang, Xijun Xu and Ling Kang

Received: 11 April 2023

Revised: 1 June 2023

Accepted: 14 June 2023

Published: 19 June 2023



**Copyright:** © 2023 by the authors. Licensee MDPI, Basel, Switzerland. This article is an open access article distributed under the terms and conditions of the Creative Commons Attribution (CC BY) license (<https://creativecommons.org/licenses/by/4.0/>).

## 1. Introduction

Li-ion batteries have become a primary secondary battery due to their characteristics of high energy density and long cycle life, which make them appealing for a variety of electronic applications [1–3]. Compared with anodes, the currently available cathodes for Li-ion batteries have a low specific capacity, which cannot meet the high energy density demand of advanced devices [4–6]. Layered Li-rich manganese oxides (LLMOs) have been the focus of much attention in the field of battery materials due to their exceptional energy storage capabilities with specific capacity above 200 mAh·g<sup>-1</sup> and operating voltage above 4.5 V vs. Li/Li<sup>+</sup> [7–13]. These compounds have the general formula, xLi<sub>2</sub>MnO<sub>3</sub>·(1 – x)LiMO<sub>2</sub>, where M represents transitional metals such as Mn, Co, and Ni [9,12,13]. However, the poor cyclic stability of LLMOs prevents their commercial applications. The dissolution of manganese from LLMOs and the electrolyte oxidation decomposition of LLMOs are mainly responsible for the poor cyclic stability of LLMOs [7,14–23]. Co-doping is effective for the cyclic stability improvement of LLMOs [23], but Co is expensive and toxic compared with Mn and Ni in LLMOs. Therefore, it remains a challenge to develop Co-free LLMOs that possess good cyclic stability.

It is known that coating LLMOs with inert compounds such as AlF<sub>3</sub>, AlBO<sub>3</sub>, P<sub>2</sub>O<sub>5</sub>, and B<sub>2</sub>O<sub>3</sub> can improve the cyclic stability of LLMOs [24–33]. These coatings separate LLMOs from direct contact with electrolytes and mitigate manganese dissolution and electrolyte decomposition, but they usually increase the interface resistance of LLMOs, which will

deteriorate the rate capability of Li-ion batteries. Comparatively, coating with CeO<sub>2</sub> is beneficial for cyclic stability and rate capability improvements in Li-ion batteries.

Due to its high electronic and ionic conductivity, cerium oxide (CeO<sub>2</sub>) has been widely used in catalysts, oxygen sensors, solid electrolytes in fuel cells, and refractory materials in thermal barrier coating [34,35]. CeO<sub>2</sub> exhibits face-centered cubic (fcc) unit cells with cations (Ce<sup>4+</sup>) and anions (O<sup>2-</sup>) occupying the octahedral interstitial sites [36]. Its ionic and electronic conductivities originate from the oxygen vacancy migration based on Ce<sup>4+</sup>/Ce<sup>3+</sup> redox [37,38] and are related to its particle size [39,40], morphology, and crystallinity [41,42]. With these features, CeO<sub>2</sub> has been used to coat the cathode of Li-ion batteries [43–46]. Several coating processes for CeO<sub>2</sub> in Li-ion batteries have been developed to date. One involves a simple dispersion of the cathode materials in a cerium-containing solution at room temperature, followed by drying and heating [44]. In this process, isolated CeO<sub>2</sub> particles will be formed, and the resultant coating layer is uneven. To improve the uniformity of the CeO<sub>2</sub> coating layer, a sol-gel process was adopted, in which chelators are required [47]. Since many factors in the sol-gel process, such as the pH value of the solution, the concentration of chelators, and temperature, affect the formation of the CeO<sub>2</sub> coating layer, it is difficult to control the physical properties of the coating layer. Researchers have utilized atomic layer deposition (ALD) to achieve a uniform coating. However, the complex equipment required by this method makes it unsuitable for large-scale applications [48].

The processes of CeO<sub>2</sub> coating involve nucleation and crystal growth of CeO<sub>2</sub>. The former determines the uniformity of the coating layer, and the latter affects the particle size of CeO<sub>2</sub>, both of which therefore determine the physical properties of the CeO<sub>2</sub> coating layer. With this knowledge, herein we propose a new strategy for coating CeO<sub>2</sub> uniformly on Co-free LLMOs, which involves a simple co-precipitation of Ce ions from aqueous solutions, followed by a low-temperature-aged process. The aqueous Ce-containing solution benefits the nucleation of CeO<sub>2</sub>, while the low-temperature-aged process favors the formation of uniform particles due to the suppression of CeO<sub>2</sub> crystal growth [39,40,49]. Thanks to the low-temperature-aged process, a uniform CeO<sub>2</sub> coating layer of 6 nm in thickness is successfully coated on LLMOs. To our knowledge, this is the first instance of applying a low-temperature-aged process for coating LLMOs, which ensures a thin and uniform coating. The resulting CeO<sub>2</sub>-coated LLMOs exhibit exceptional cyclic stability and rate capability, showing an improved cycle capacity retention of 85% after 100 cycles (compared to 67% for the uncoated sample) and an increased rate capacity retention of 23% at 5 C/0.05 C (compared to 10% for the uncoated sample). These outcomes demonstrate the notable benefits of the coating treatment on the performance of the LLMOs.

## 2. Materials and Methods

### 2.1. Sample Preparation

Co-free Li-rich oxide, Li<sub>1.2</sub>Ni<sub>0.2</sub>Mn<sub>0.6</sub>O<sub>2</sub>, was synthesized by the co-precipitation method. Typically, a solution was prepared by dissolving 1.32 g manganese sulfate (MnSO<sub>4</sub>·H<sub>2</sub>O) and 0.76 g nickel nitrate (Ni(NO<sub>3</sub>)<sub>2</sub>·6H<sub>2</sub>O) in deionized water with a molar ratio of Mn:Ni = 3:1, followed by dropwise addition of excessive NaOH solution under constant stirring at 50 °C. The ammonium aqueous solution was utilized to maintain a pH value of 11.5 during the co-precipitation process. The precipitated precursor Ni<sub>0.2</sub>Mn<sub>0.6</sub>(OH)<sub>x</sub> was filtered, washed with deionized water, and vacuum dried at 105 °C for 8 h. The obtained powders were mixed with 0.69 g LiOH·H<sub>2</sub>O, which represents an excess of 5 wt.% Li compared to the stoichiometric Li<sub>1.2</sub>Ni<sub>0.2</sub>Mn<sub>0.6</sub>O<sub>2</sub>, followed by calcining at 450 °C for 4 h and 900 °C for 15 h with a 3 °C min<sup>-1</sup> heating rate in air, to obtain Li-rich oxide, denoted as LMN-P.

The preparation of CeO<sub>2</sub>-coated Co-free Li-rich oxide, denoted as LMN-C, is illustrated in Figure 1. First, 1.00 g of the obtained LMN-P powder and 0.06 g of Ce(NO<sub>3</sub>)<sub>3</sub>·6H<sub>2</sub>O were dispersed into deionized water ultrasonically for 30 min. Second, the aforementioned solution was supplemented with an appropriate amount of ammonium aqueous solution under 100 °C, followed by quickly cooling to 0 °C and subsequently aging at 0 °C for 24 h.

To obtain LMN-C, the precipitated product was filtered, washed with deionized water, vacuum-dried for 8 h at 105 °C, then calcined at 650 °C for 5 h in air.

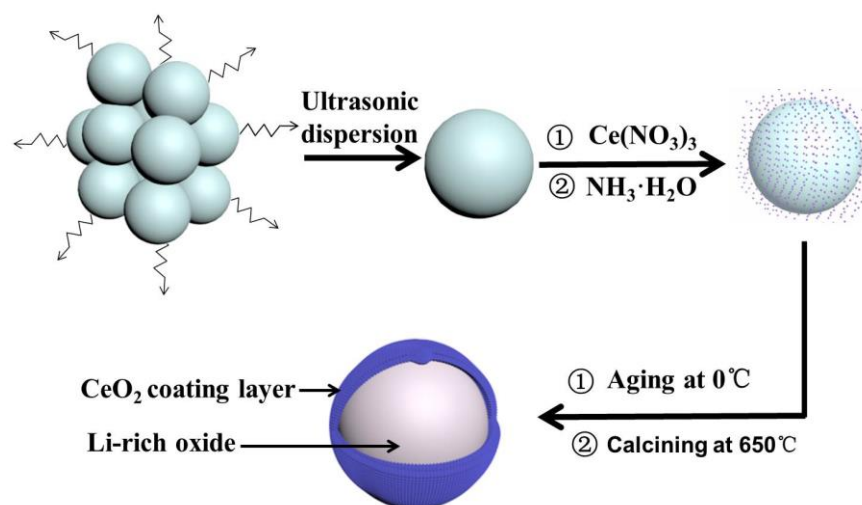


**Figure 1.** Illustration of low-temperature-aged synthesis of CeO<sub>2</sub>-coated Li-rich oxide.

## 2.2. Physical Characterization

The SHI-MADZU X-ray diffractometer XRD-6100 was used to characterize the crystalline structure of the resulting samples, with a data collection range of 10–80° in 2θ, an interval of 0.02°, and a scanning rate of 2° min<sup>-1</sup>. The collected XRD data was refined using MDI Jade 6 software to obtain the corresponding XRD patterns [50]. To characterize the effect of the coating, the morphology of the LMN-P and LMN-C samples before and after cycling was observed by ZEISS Ultra 55 scanning electron microscopy (SEM) and JEM-2100HR transmission electron microscopes (TEM). The surface composition was analyzed by Bruker Tensor 27 FTIR, made in Germany. The contents of elements on the lithium anode were analyzed by an Energy Dispersive Spectrometer (EDS) (JEM-2100HR) and inductively coupled plasma (ICP) (Huake, 8100). The elemental composition and chemical states of the resulting sample surface were characterized by X-ray photoelectron spectroscopy (XPS, Thermo Scientific™ (Waltham, MA, USA) K-Alpha™+). The tests were carried out under vacuum ( $p < 10^{-8}$  mbar) with a monochromatic Al Kα X-ray source (1486.6 eV), operating power of 100 W, and pass energy of 150 eV (survey scans) or 25 eV (high-resolution scans). The peak fitting process was performed using the XPSPEAK41 software, with the C 1s peak binding energy of 284.3 eV as the standard reference [35,50]. To characterize the cycled electrodes, they were obtained from the disassembled cycled button cells, then rinsed three times using anhydrous DMC solvent. Subsequently, the sample was vacuum dried at room temperature overnight. All these processes were carried out in a glovebox with an inert argon atmosphere.

## 2.3. Electrochemical Measurements

The electrodes were prepared by mixing LMN-P/LMN-C, conductive carbon, and polyvinylidene fluoride with a ratio of 8:1:1, then coating the mixing slurry on the Al foil, followed by ambient pressure drying at 85 °C and vacuum drying at 120 °C. The electrolyte with 1.0 M/L LiPF<sub>6</sub> in EC/EMC/DEC (1:1:1 wt.%) was purchased from Dongguan Kaixin Battery Material Co., Ltd., Dongguan, China. The separator was purchased from Celgard and vacuum-dried before use. For electrochemical measurements, the 2032 button cells were assembled in a highly pure Ar-filled glove box by employing the prepared electrodes as the working electrode, Li metal as the counter electrode, purchased electrolyte as the supporting electrolyte, and the dried Celgard's membrane as the separator. The cyclic voltammetry was performed with a scan rate of 0.2 mV s<sup>-1</sup> in the voltage range of 2.0–5.0 V (vs. Li/Li<sup>+</sup>), and the electrochemical impedance was tested from 0.01 Hz to 10<sup>6</sup> Hz with a

5 mV amplitude. Both were carried out on the CHI test system. The land test system was utilized to carry out the charge-discharge tests. To guarantee the precision of the obtained results, three tests were performed for each sample, and the mean of one of the three tests was used for discussion in this work.

### 3. Results and Discussions

#### 3.1. Structure and Morphology

The XRD patterns of LMN-P and LMN-C are presented in Figure 2. For LMN-P, all peaks can be indexed to the trigonal  $\alpha$ - $\text{NaFeO}_2$  structure with R-3m symmetry (PDF#89-3601) and monoclinic  $\text{Li}_2\text{MnO}_3$  with C2/m symmetry (PDF#84-1634). Specifically, the broad diffraction peaks of (020) and (110) between  $20^\circ$  and  $25^\circ$  are the key characteristics of weak superstructure diffractions for the arrangements of metal cations ( $\text{Li}^+$  and  $\text{Mn}^{4+}$ ) present in the transition metal layer [10,51]. Compared with LMN-P, a very weak peak corresponding to the fluorite structure phase of  $\text{CeO}_2$  (PDF#34-0394) appears in LMN-C, indicating that  $\text{CeO}_2$  has been successfully coated on Li-rich oxide. Usually, the components with low contents in the sample are difficult to detect by XRD. In LMN-C,  $\text{CeO}_2$  is detected by XRD at a very low intensity, which should be ascribed to the good crystallization of  $\text{CeO}_2$ . The peaks of (111), (200), (220), and (311) in LMN-C demonstrate that the resulting  $\text{CeO}_2$  exhibits a center-facing cubic structure with high crystallinity. Notably, both LMN-P and LMN-C exhibit low  $\text{Li}^+$  and  $\text{Ni}^{2+}$  cation disordering, as evidenced by their  $I(003)/I(104)$  ratios of 1.59 and 1.62, respectively [52]. In addition, the sharp split peaks in (006)/(012) and (018)/(110) in both samples further confirm the layer structure with good crystallinity [19,41,44]. The XRD patterns of the layered LMN-P and LMN-C suggest that pure samples with good crystal structure and low  $\text{Li}^+$  and  $\text{Ni}^{2+}$  disordering were obtained, and the introduction of the  $\text{CeO}_2$  coating layer does not change the crystal structure of Li-rich oxide.

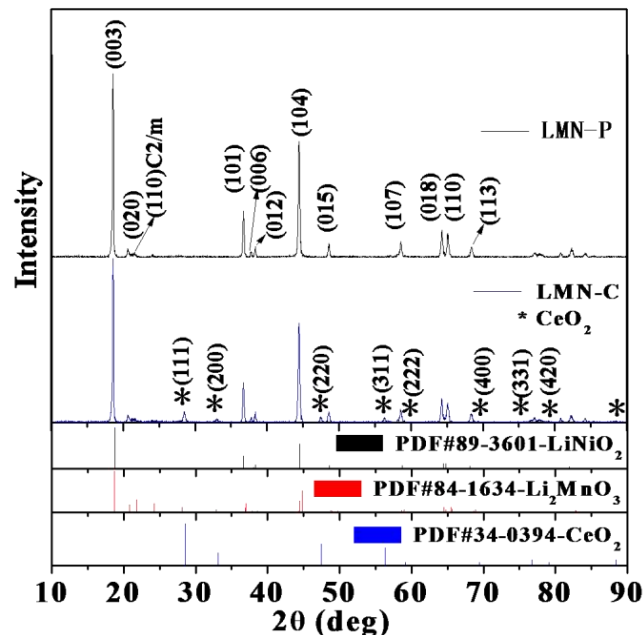


**Figure 2.** XRD patterns of pristine  $\text{Li}_{1.2}\text{Ni}_{0.2}\text{Mn}_{0.6}\text{O}_2$  (LMN-P) and  $\text{CeO}_2$ -coated  $\text{Li}_{1.2}\text{Ni}_{0.2}\text{Mn}_{0.6}\text{O}_2$  (LMN-C).

Figure 3 shows the SEM and TEM images of the LMN-P and LMN-C. Based on Figure 3A,B, it appears that there are no observable distinctions in morphology or particle size between LMN-P and LMN-C. A smooth and clean surface can be observed for LMN-P particles. The surface of LMN-C is slightly rougher than that of LMN-P. Furthermore, LMN-C presents an extra uniform and compact coating layer of about 6 nm thick compared with LMN-P, as shown in Figure 3C,D. The presence of a  $\text{CeO}_2$  coating can be further

confirmed by TEM, as shown in Figure S1. Apparently, the simple low-temperature-aged process can effectively realize a uniform and compact  $\text{CeO}_2$  coating for Li-rich oxide. The implementation of this uniform and compact  $\text{CeO}_2$  coating layer effectively prevents the dissolution of metal ions from the LLMOs and the degradation of electrolytes through decomposition [45,53].

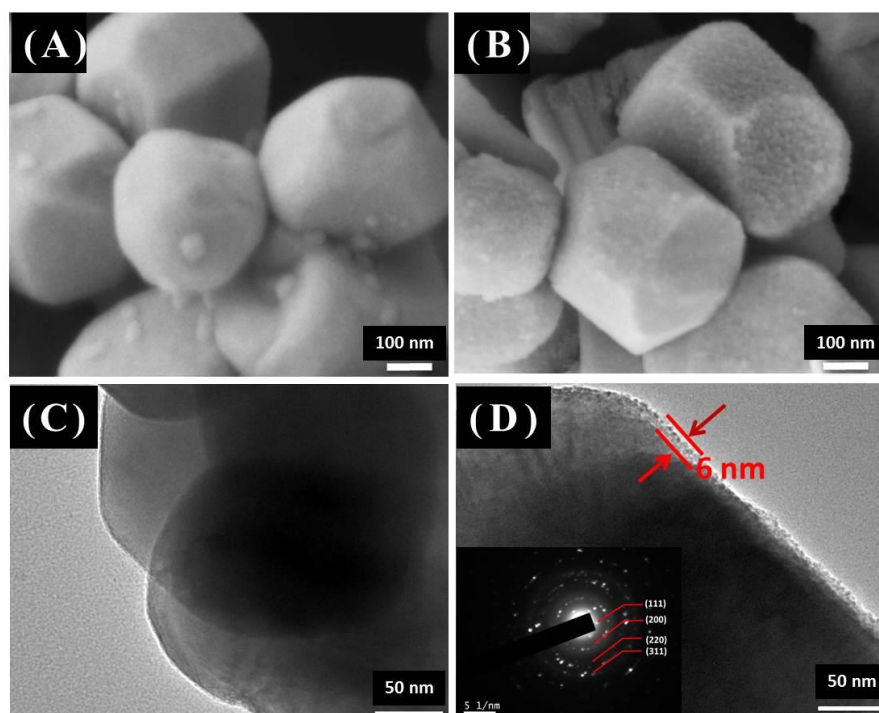


**Figure 3.** SEM images of LMN-P (A) and LMN-C (B); TEM images of LMN-P (C) and LMN-C with an insertion of selected area electron diffraction (SAED) (D).

### 3.2. Electrochemical Performances

Cyclic voltammograms of LMN-P and LMN-C are shown in Figure 4. During forward scanning in the 1st cycle, the LMN-P electrode exhibits two coalescent oxidation peaks below 4.40 V (vs.  $\text{Li}/\text{Li}^+$ ), as presented in Figure 4A. These peaks are attributed to the oxidations of nickel ions in different chemical environments, namely in  $\text{LiMO}_2$ -like ( $M = \text{Ni}, \text{Mn}$ ) and  $\text{Li}_2\text{MnO}_3$ -like ( $\text{LiM}_6$ ) components [54]. During the charging process, a major peak of oxidation current is observed, starting at 4.40 V (vs.  $\text{Li}/\text{Li}^+$ ) and reaching its maximum at 4.81 V (vs.  $\text{Li}/\text{Li}^+$ ), which can be explained by the concurrent lithium and oxygen extraction from  $\text{Li}_2\text{MnO}_3$  and the structural reorganization where transition metal cations occupy the available oxygen vacancies in  $\text{LiMnO}_3$  [13,55]. These processes are irreversible and cannot be identified in the discharge process.

In the first cycle, the irreversible oxygen loss and the rearrangement of  $\text{LiMnO}_3$  structure result in the disappearance of the oxidation peak at above 4.70 V (vs.  $\text{Li}/\text{Li}^+$ ) in subsequent cycles, as shown in Figure 4B. In the backward scanning, the reduction peak located around 3.60 V (vs.  $\text{Li}/\text{Li}^+$ ), corresponding to the reduction of  $\text{Ni}^{4+}$  to  $\text{Ni}^{2+}$  [8,10–13,54], can be identified, as shown in Figure 4A. Additionally, a small reduction current appears at  $\sim 3.30$  V (vs.  $\text{Li}/\text{Li}^+$ ) in the 1st cycle, and this reduction peak becomes more significant for the subsequent cycles, as shown in Figure 4B. These observed changes imply that the electronic environment of manganese ions is notably affected by the structural rearrangement resulting from irreversible oxygen loss, highlighting the significant role of the  $\text{Mn}^{4+}/\text{Mn}^{3+}$  reaction during the electrochemical cycling process [55].

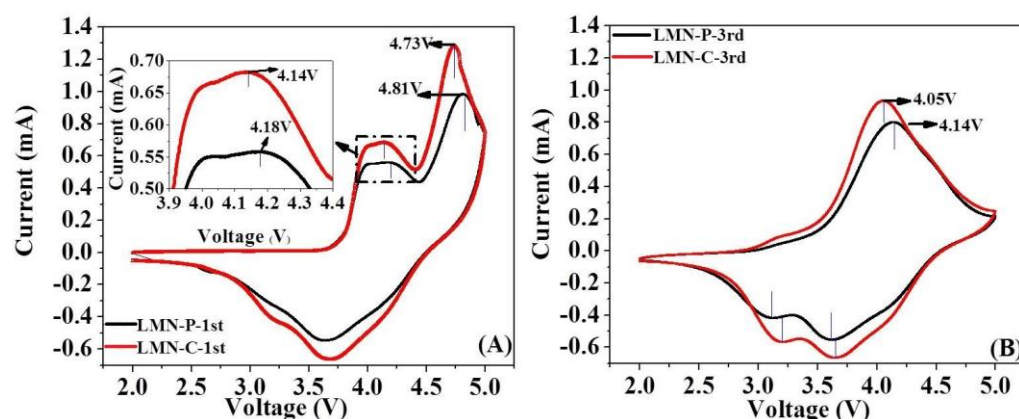


**Figure 4.** Cyclic voltammograms of LMN-P and LMN-C for the first (A) and third (B) cycles at a scan rate of  $0.2 \text{ mV s}^{-1}$ .

After the LLMOs are coated with  $\text{CeO}_2$ , the peak potentials for the oxidation of nickel ions and the irreversible reaction of  $\text{Li}_2\text{MnO}_3$  in the first cycle shift negatively to 4.14 V (vs.  $\text{Li}/\text{Li}^+$ ) and 4.73 V (vs.  $\text{Li}/\text{Li}^+$ ), respectively (Figure 4A). Correspondingly, the oxidation peak shifts towards negative and the reduction peak shifts towards positive values for  $\text{Ni}^{2+}/\text{Ni}^{4+}$  reactions in the following cycles (Figure 4B). This can be attributed to the better  $\text{Li}^+$  diffusion path generated by the rearrangement of the  $\text{Li}_2\text{MnO}_3$  component during the first cycle. Additionally, all the reaction currents increase due to the  $\text{CeO}_2$  coating. These results suggest that the  $\text{CeO}_2$  coating increases the reversibility of the electrochemical redox of Li-rich oxide, which can be ascribed to the electronically and ionically conductive properties of  $\text{CeO}_2$ .

To further demonstrate the electrochemical performances of LMN-P and LMN-C, charge/discharge tests and electrochemical impedance spectroscopy were performed using button cells. Figure 5 illustrates the results of the investigation. Figure 5A presents the cyclic stability at 0.1 C ( $1 \text{ C} = 200 \text{ mA g}^{-1}$ ) after an activation process with 0.05 C for 4 cycles between 2.0 and 4.8 V (vs.  $\text{Li}/\text{Li}^+$ ). Figure 5A reveals that LMN-P has poor cyclic stability, as evidenced by the decreased discharge capacity, which went from  $191 \text{ mAh g}^{-1}$  to  $127 \text{ mAh g}^{-1}$  over 100 cycles, with capacity retention of only 67%. This is the primary issue that limits the applicability of Li-rich oxide, which is attributed to the unprotected interface between LMN-P and the electrolyte, where transition metal ion dissolution and electrolyte decomposition may occur. LMN-C, in comparison, has a significantly higher cyclic stability performance with a discharge capacity decrease from  $200 \text{ mAh g}^{-1}$  to  $170 \text{ mAh g}^{-1}$  and a capacity retention of 85% after 100 cycles. Apparently, the low-temperature-aged process ensures a uniform  $\text{CeO}_2$  coating layer that efficiently protects Li-rich oxide from dissolution and prevents electrolyte decomposition, resulting in significantly improved cyclic stability of Li-rich oxide.

The charge/discharge performance of both samples is similar, as illustrated by the initial charge/discharge curves (0.05 C, Figure 5B). There are two potential plateaus at around 4.10 and 4.50 V (vs.  $\text{Li}/\text{Li}^+$ ), respectively, which correspond to the oxidation of  $\text{Ni}^{2+}/\text{Ni}^{4+}$  and the irreversible oxygen loss from the layered lattice. This similarity suggests that the  $\text{CeO}_2$  coating does not change the intrinsic electrochemical property of Li-rich oxide, which is in agreement with the same crystal structure of LMN-C as LMN-P. Differently, LMN-C displays a slightly lower charge potential plateau and a slightly higher discharge potential plateau, suggesting that LMN-C has less polarization for lithiation/delithiation kinetics than LMN-P. This decreased polarization of LMN-C can be ascribed to the electronically and ionically conductive properties of the  $\text{CeO}_2$  coating [48]. The lower polarization of LMN-C allows for a higher initial discharge capacity ( $226 \text{ mAh g}^{-1}$ ) compared to LMN-P ( $208 \text{ mAh g}^{-1}$ ). As cycling proceeds, the difference in polarization between two samples becomes more significant, as shown in Figure 5C, suggesting that the interface between

Li-rich oxide and electrolyte is deteriorated by the transition metal ions dissolution and the electrolyte's decomposition for LMN-P, which can be mitigated by CeO<sub>2</sub> coating.

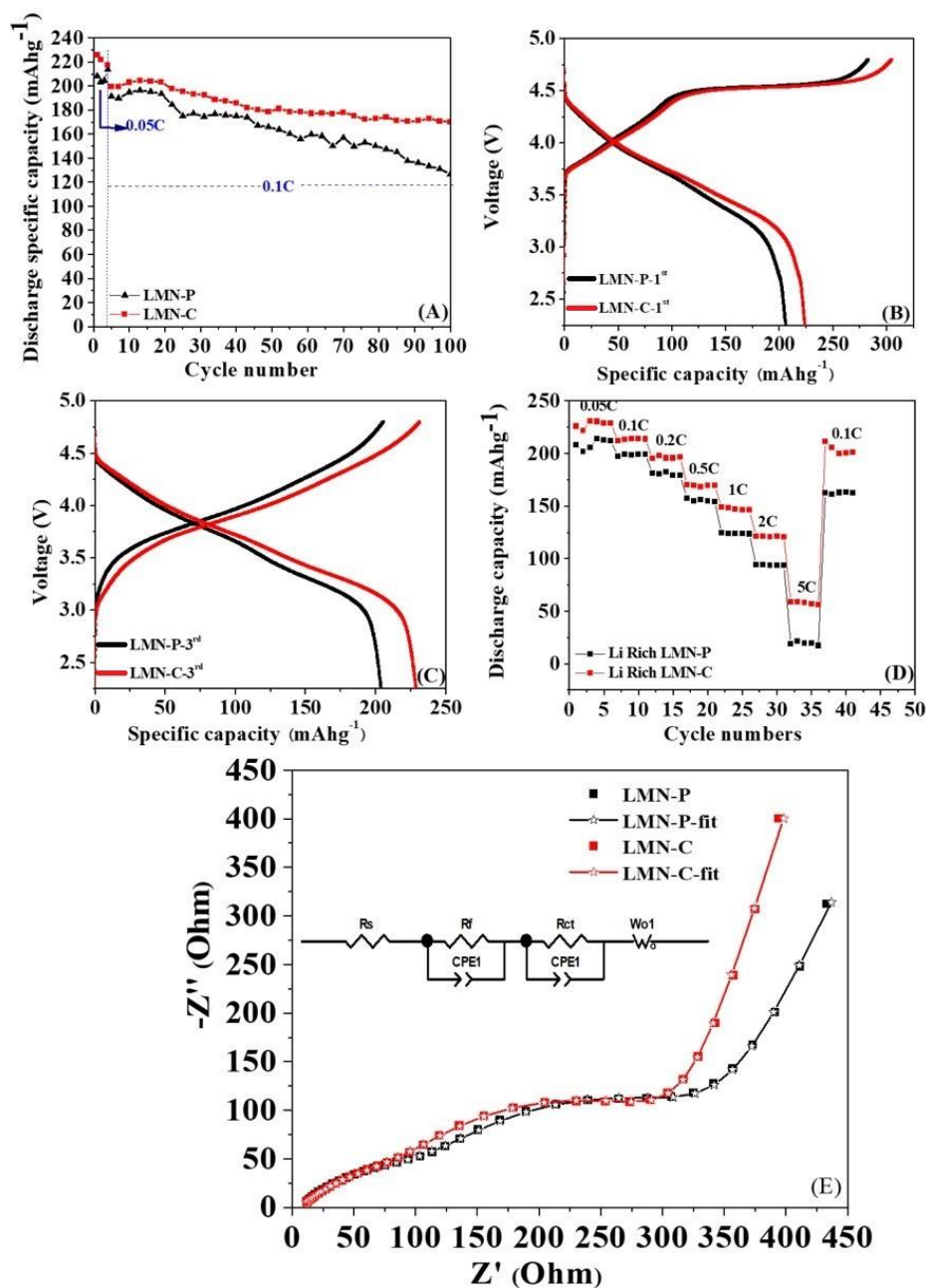


**Figure 5.** Cycling stability (A), charge/discharge curves for the 1st (B) and the 3rd (C) cycles with a current density of 10 mA g<sup>-1</sup>, rate capability (D), and (E) electrochemical impedance spectra with the equivalent circuit for fitting of the assembled cell for LMN-P and LMN-C.

With its lower polarization, LMN-C exhibits better rate capability than LMN-P, as shown in Figure 5D. At 0.05, 0.1, 0.2, 0.5, 1, 2, and 5 C, LMN-P delivers 213 mAh g<sup>-1</sup>, 199 mAh g<sup>-1</sup>, 181 mAh g<sup>-1</sup>, 154 mAh g<sup>-1</sup>, 124 mAh g<sup>-1</sup>, 94 mAh g<sup>-1</sup>, and 21 mAh g<sup>-1</sup>, with the rate of capacity retention (n/0.05 C, n = 0.1, 0.2, 0.5, 1, 2, and 5 C) being 93%, 85%, 72%, 58%, 44%, and 10%, respectively. Comparatively, LMN-C delivers 229 mAh g<sup>-1</sup>, 213 mAh g<sup>-1</sup>, 198 mAh g<sup>-1</sup>, 170 mAh g<sup>-1</sup>, 149 mAh g<sup>-1</sup>, 121 mAh g<sup>-1</sup>, and 59 mAh g<sup>-1</sup>, with the rate of capacity retention being 93%, 86%, 74%, 65%, 53%, and 23%, respectively. Below 0.5 C, there is little difference in the rate of capacity retention between the two samples. However, an obvious difference appears as the discharge rates increase. This

phenomenon can be explained by the contribution of the electronic and ionic conductivity of CeO<sub>2</sub>, which plays a more important role in lithiation/delithiation kinetics at higher rates [47]. Noticeably, the LMN-C exhibits higher discharge capacity for all rates, which can be ascribed to the CeO<sub>2</sub>/s oxygen storage capability that reduces the irreversible consumption of Li and oxygen loss in the Li<sub>2</sub>MnO<sub>3</sub> component. In addition, the LMN-C exhibits more decent capacity recovery than the LMN-P after high-rate discharge, suggesting that the CeO<sub>2</sub>-coated layer is beneficial for keeping the structure stability of Li-rich oxide.

Electrochemical impedance spectra obtained from fresh button cells are shown in Figure 5E. In the spectra, two compressed semicircles were observed at high frequencies, while a straight slope line was observed at low frequencies. The first compressed semicircle corresponds to film resistance ( $R_f$ ) of the electrode/electrolyte, the second one is corresponding to the charge transfer resistance ( $R_{ct}$ ) of reaction, and the slope line is ascribed to the Li<sup>+</sup> ion diffusion in the Li-rich electrode ( $W_{oi}$ ). Table 1 lists the values obtained by fitting the equivalent circuit shown in Figure 5E, indicating a reduction of  $R_f$  and  $R_{ct}$  from 106  $\Omega$  to 93  $\Omega$  and 181  $\Omega$  to 172  $\Omega$ , respectively, after the introduction of the CeO<sub>2</sub> coating layer. These decreased interfacial resistances explain the improved rate capability of LMN-C.

**Table 1.** Charge transfer and film resistances of LMN-P and LMN-C.

Resistance/ $\Omega$	Charge Transfer ( $R_{ct}$ )	Film ( $R_f$ )
LMN-P	181	106
LMN-C	172	93

In order to confirm the impact of CeO<sub>2</sub> on the performance of LLMOs, the cycled LMN-P and LMN-C electrodes were characterized by SEM, TEM, FTIR, and XRD. The obtained results are presented in Figure 6. After cycling, LMN-P is apparently covered with a thick deposit (Figure 6A) and the well-crystallized particles observed from Figure 3C cracks are highlighted in Figure 6C with the use of red arrows, confirming that severe electrolyte decomposition and particle separation happen on the unprotected Li-rich oxide. Differently, less deposit is observed (Figure 6B) and well-crystallized particles covered with a CeO<sub>2</sub> coating layer are maintained (Figure 6D) for the cycled LMN-C electrode. Obviously, the CeO<sub>2</sub> coating layer provides an effective separation between the electrolyte and Li-rich oxide, suppressing electrolyte decomposition and maintaining the integrity of Li-rich oxide. The FTIR spectrum of the cycled electrode is shown in Figure 6E. The peaks approximately at 840, 1066, 1175, 1230, and 1398 cm<sup>-1</sup>, which are ascribed to the PVDF [56–59], are stronger for LMN-C, demonstrating that there are less electrolyte decomposition products on LMN-C than LMN-P, which is in agreement with the results of SEM and TEM analysis. The peaks at 1626 and 1734 cm<sup>-1</sup> in LMN-P represent the C=O and C-O of polycarbonates, such as poly RO-CH<sub>2</sub>CH<sub>2</sub>OCO<sub>2</sub><sup>-</sup>, resulting from the electrolyte decomposition [58,60,61]. However, these two peaks vanish in LMN-C, confirming that CeO<sub>2</sub> can effectively suppress the decomposition of electrolytes. It is worth noting that CeO<sub>2</sub> is not detected for LMN-C by FTIR, which can be explained by the insensitivity of inorganic compounds with low contents in the sample to FTIR.

From the XRD patterns of the cycled electrodes (Figure 6F), the main diffraction peaks of Li-rich oxide (in Figure 2) remain, and new peaks appear at 65° and 78° for both cycled electrodes, which belong to the current collector (aluminum). However, LMN-P changes the strongest diffraction peak from crystal face (003) (in Figure 2) to (104) (in Figure 6F), while LMN-C maintains the same peak position and intensity. Because of the strong diffraction from the aluminum current collector, the most intensive (003) reflection peak for the pristine materials, as recorded in Figure 2, becomes weaker for the cycled electrodes. This peak remains most intense for the cycled LMN-C but becomes weaker than the peak at (104) for the cycled LMN-P, indicating that the LMN-C maintains its crystal structure better than the LMN-P, which experiences more significant degradation. Table 2 presents the lattice parameters of the primary phase for both samples, both before and after cycling. After

cycling, C2/m, represented by  $\text{Li}_2\text{MnO}_3$ , disappears because of its activation [62,63], while R-3m of LMN-P shows a larger change in size than that of LMN-C, corresponding to the more serious deterioration of LMN-P.

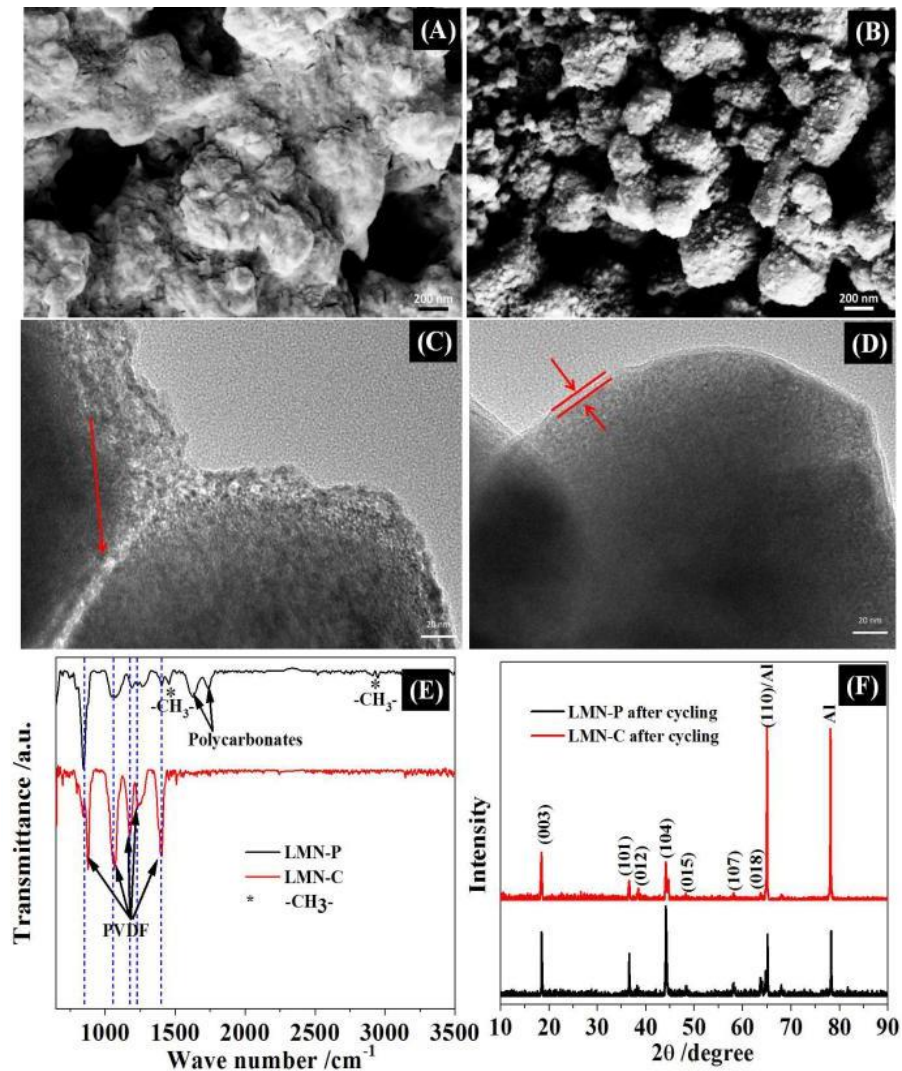


**Figure 6.** SEM and TEM images of LMN-P (A,C) and LMN-C (B,D); FTIR spectra (E) and XRD patterns (F) of LMN-P and LMN-C electrodes after cycling tests.

**Table 2.** Lattice parameters of LMN-P and LMN-C before and after cycling.

Sample		R-3m		C2/m		
		a (Å)	b (Å)	a (Å)	b (Å)	c (Å)
Before cycling	LMN-P	2.8611	14.25785	4.9586	8.57046	5.03293
After cycling	LMN-C	2.8635	14.25752	4.9559	8.54779	5.03707
Before cycling	LMN-P	2.87467	14.43984			
After cycling	LMN-C	2.87601	14.26065			

The transport and deposition of the transition metal ions from the cathode to the anode can be detected by ZAF-corrected EDS and ICP. Figure 7 and Tables S1 and S2 present the surface morphology and element contents of the lithium anodes from the cycled cells with LMN-P and LMN-C as cathodes. The lithium anode of the cell with LMN-P (Figure 7A) is coarser than that with LMN-C (Figure 7E), suggesting that more severe electrolyte decomposition happens on the anode in the cell with Li/LMN-P [64]. The EDS and ICP results (Figure 7B–H, Tables S1 and S2) show that both anodes contain C, O, F, P,

and Mn, but the contents of these elements are different. C and O come from the solvent decomposition on the lithium anode. The smaller contents of C and O on the lithium anode for LMN-C than those for LMN-P can be explained by the thinner deposit layer on the anode for LMN-C. P comes from  $\text{LiPF}_6$  decomposition. The far larger content of P on the lithium anode for LMN-P than that for LMN-C can be ascribed to the more severe electrolyte decomposition on the anode for LMN-P. Mn and Ni are from the dissolution of the cathode, as reported by other researchers [65,66]. The contents of Mn and Ni on the anode for LMN-P are far larger than those for LMN-C, which are responsible for the more severe electrolyte decomposition on the anode for LMN-P and confirm that LMN-C is structurally more stable than LMN-P. Apparently, the  $\text{CeO}_2$  coating layer suppresses Mn and Ni dissolution from Li-rich oxide, which is important for battery performance improvement [67].

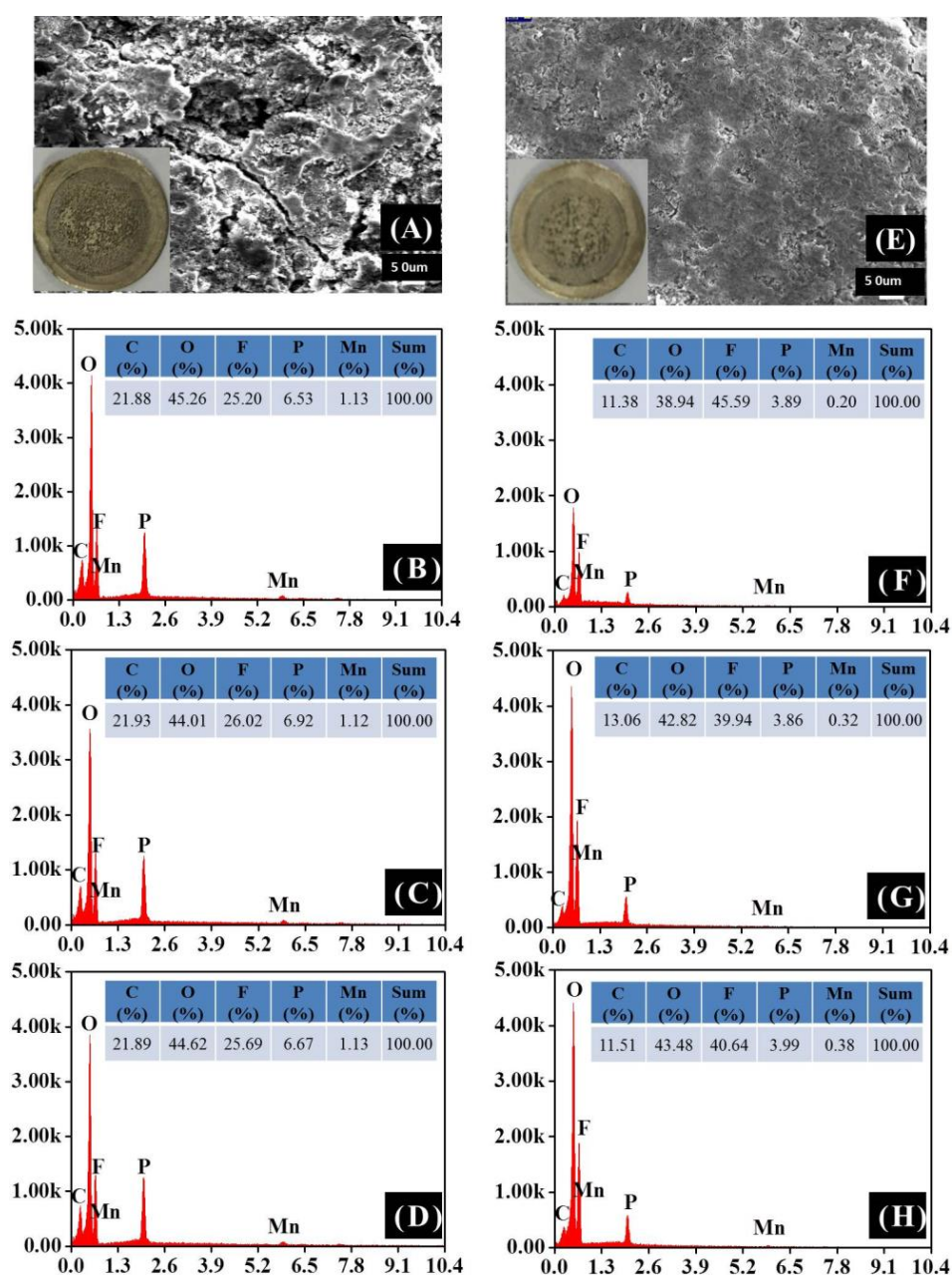


Figure 7. SEM images and EDS of lithium electrodes from the cycled cells with LMN-P (A–D) and LMN-C (E–H).

XPS analysis can be used to provide further confirmation of the protective effect of the CeO<sub>2</sub> coating layer on the surface of the Li-rich oxide. The XPS patterns of the LMN-P and LMN-C electrodes after 100 cycles at the voltage range of 2.0–4.8 V are presented in Figure S2. The C 1s spectrum reveals several peaks: the peak located at 284.3 eV is attributed to the conductive carbon [68,69], while the peaks at 285.6 eV and 290.8 eV are assigned to the C-H bond and C-F bond in the PVDF binder. Additionally, the peak at 265.5 eV is associated with the C-O bond, the peak at 288.6 eV with the C=O bond, the peak at 289.9 eV with the OCO<sub>2</sub> bond, and the peak at 284.9 eV with polycarbonates, respectively [66–70]. Comparatively, the observation of a weaker intensity of PVDF bond, along with the stronger C-O and OCO<sub>2</sub> peaks in the LMN-P sample, can be attributed to more severe electrolyte decomposition, which causes thicker deposits to form on the electrode [61,71,72]. This difference can also be observed from the M-O bond and C-O bond in the O 1s spectrum, as well as the peak at 136.8 eV corresponding to Li<sub>x</sub>PF<sub>y</sub> in the P 2p spectrum [73,74]. These observations further confirm that the CeO<sub>2</sub> coating layer can effectively protect the Li-rich oxide and suppress the electrolyte decomposition of the Li-rich oxide.

#### 4. Conclusions

This study introduces a novel method for synthesizing CeO<sub>2</sub>-coated Li-rich oxides in which a uniform CeO<sub>2</sub> coating layer is achieved with a low-temperature-aged process. Due to the ionic conductivity of CeO<sub>2</sub> and its inertness to electrolyte decomposition, the CeO<sub>2</sub> coating layer not only provides protection for Li-rich oxides from structural collapse but also reduces the interfacial resistance between the Li-rich oxide material and the electrolyte. With these contributions, the as-synthesized CeO<sub>2</sub>-coated Li-rich oxide exhibits enhanced performance as a cathode material for Li-ion batteries, with notable improvements in both rate capability and cyclic stability. Thus, this low-temperature-aged process provides a promising strategy to address the challenges remaining in the practical utilization of Li-rich oxide materials, not limited to Co-free Li-rich oxide.

**Supplementary Materials:** The following supporting information can be downloaded at: <https://www.mdpi.com/article/10.3390/batteries9060330/s1>, Figure S1: TEM image (A) and corresponding EDS elemental mapping of Ce (B), TEM image (C) and selected area electron diffraction (SAED) of CeO<sub>2</sub> (D) for CeO<sub>2</sub> coated Li<sub>1.2</sub>Ni<sub>0.2</sub>Mn<sub>0.6</sub>O<sub>2</sub> without the low-temperature-aged coating process; Figure S2: XPS of the cycled LMN-P and LMN-C electrodes; Table S1: EDS of lithium electrodes from the cycled cells with LMN-P and LMN-C; Table S2: ICP analysis for Mn and Ni of the lithium electrodes from the cycled cells with LMN-P and LMN-C.

**Author Contributions:** Conceptualization, Y.L. and W.L.; methodology, Y.L., B.L. and W.L.; software, Y.L. and B.L.; validation, M.C. and W.L.; formal analysis, Y.L. and W.L.; investigation, Y.L.; resources, W.L.; data curation, Y.L. and W.L.; writing—original draft preparation, Y.L.; writing—review and editing, Y.L., B.L. and W.L.; visualization, Y.L.; supervision, W.L.; project administration, W.L.; funding acquisition, Y.L. and W.L. All authors have read and agreed to the published version of the manuscript.

**Funding:** This research was funded by the National Natural Science Foundation of China (Grant numbers 22005063, and 22202078) and the Department of Education of Guangdong Province (Grant number 2020KQNCX082).

**Data Availability Statement:** Not applicable.

**Conflicts of Interest:** The authors declare no conflict of interest.

#### References

1. Li, Z.; We, X.; Yang, Z. Pulsed laser 3D-micro/nanostructuring of materials for electrochemical energy storage and conversion. *Prog. Mater. Sci.* **2023**, *133*, 101052. [[CrossRef](#)]
2. Grey, C.P.; Hall, D.S. Prospects for lithium-ion batteries and beyond—A 2030 vision. *Nat. Commun.* **2020**, *11*, 6279. [[CrossRef](#)]
3. Wu, K.; Cui, J.; Yi, J.; Liu, X.; Ning, F.; Liu, Y.; Zhang, J. Biodegradable Gel Electrolyte Suppressing Water-Induced Issues for Long-Life Zinc Metal Anodes. *ACS Appl. Mater. Interfaces* **2022**, *14*, 34612–34619. [[CrossRef](#)] [[PubMed](#)]

4. Molaiyan, P.; Reis, G.S.D.; Karuppiah, D.; Subramaniyam, C.M.; Flaviano, G.A.; Lassi, U. Recent Progress in Biomass-Derived Carbon Materials for Li-Ion and Na-Ion Batteries—A Review. *Batteries* **2023**, *9*, 116. [[CrossRef](#)]
5. Andre, D.; Kim, S.J.; Lamp, P.; Lux, S.F.; Maglia, F.; Paschos, O.; Stiaszny, B. Future generations of cathode materials: An automotive industry perspective. *J. Mater. Chem. A* **2015**, *3*, 6709–6732. [[CrossRef](#)]
6. Li, B.; Wang, Y.; Tu, W.; Wang, Z.; Xu, M.; Xing, L.; Li, W. Improving cyclic stability of lithium nickel manganese oxide cathode for high voltage lithium ion battery by modifying electrode/electrolyte interface with electrolyte additive. *Electrochim. Acta* **2014**, *147*, 636–642. [[CrossRef](#)]
7. Rozier, P.; Tarascon, J.M. Review—Li-Rich Layered Oxide Cathodes for Next-Generation Li-Ion Batteries: Chances and Challenges. *J. Electrochem. Soc.* **2015**, *162*, A2490. [[CrossRef](#)]
8. Fang, L.; Chen, M.; Nam, K.W.; Kang, Y.M. Redox Evolution of Li-Rich Layered Cathode Materials. *Batteries* **2022**, *8*, 132. [[CrossRef](#)]
9. Thackeray, M.M.; Kang, S.; Johnson, C.S.; Vaughey, J.T.; Benedek, R.; Hackney, S.A. Li<sub>2</sub>MnO<sub>3</sub>-stabilized LiMO<sub>2</sub> (M = Mn, Ni, Co) electrodes for lithium-ion batteries. *J. Mater. Chem.* **2007**, *17*, 3112–3125. [[CrossRef](#)]
10. Thackeray, M.M.; Johnson, C.S.; Vaughey, J.T.; Li, N.; Hackney, S.A. Advances in manganese-oxide ‘composite’ electrodes for lithium-ion batteries. *J. Mater. Chem.* **2005**, *15*, 2257–2267. [[CrossRef](#)]
11. Chen, D.; Yu, Q.; Xiang, X.; Chen, M.; Chen, Z.; Song, S.; Xiong, L.; Liao, Y.; Xing, L.; Li, W. Porous layered lithium-rich oxide nanorods: Synthesis and performances as cathode of lithium ion battery. *Electrochim. Acta* **2015**, *154*, 83–93. [[CrossRef](#)]
12. Armstrong, A.R.; Holzapfel, M.; Novák, P.; Johnson, C.S.; Kang, S.; Thackeray, M.M.; Bruce, P.G. Demonstrating Oxygen Loss and Associated Structural Reorganization in the Lithium Battery Cathode Li[Ni<sub>0.2</sub>Li<sub>0.2</sub>Mn<sub>0.6</sub>]O<sub>2</sub>. *J. Am. Chem. Soc.* **2006**, *128*, 8694–8698. [[CrossRef](#)]
13. Xiang, X.; Li, X.; Li, W. Preparation and characterization of size-uniform Li[Li<sub>0.131</sub>Ni<sub>0.304</sub>Mn<sub>0.565</sub>]O<sub>2</sub> particles as cathode materials for high energy lithium ion battery. *J. Power Sources* **2013**, *230*, 89–95. [[CrossRef](#)]
14. Ji, X.; Xia, Q.; Xu, Y.; Feng, H.; Wang, P.; Tan, Q. A review on progress of lithium-rich manganese-based cathodes for lithium ion batteries. *J. Power Sources* **2021**, *487*, 229362. [[CrossRef](#)]
15. Zuo, W.; Luo, M.; Liu, X.; Wu, J.; Liu, H.; Li, J.; Winter, M.; Fu, R.; Yang, W.; Yang, Y. Li-rich cathodes for rechargeable Li-based batteries: Reaction mechanisms and advanced characterization techniques. *Energy Environ. Sci.* **2020**, *13*, 4450–4497. [[CrossRef](#)]
16. Xiang, X.; Li, W. Significant influence of insufficient lithium on electrochemical performance of lithium-rich layered oxide cathodes for lithium ion batteries. *Electrochim. Acta* **2014**, *133*, 422–427. [[CrossRef](#)]
17. Lee, S.H.; Moon, J.S.; Lee, M.S.; Yu, T.H.; Kim, H.; Park, B.M. Enhancing phase stability and kinetics of lithium-rich layered oxide for an ultra-high performing cathode in Li-ion batteries. *J. Power Sources* **2015**, *281*, 77–84. [[CrossRef](#)]
18. Ramakrishnan, S.; Park, B.; Wu, J.; Yang, W.; McCloskey, B.D. Extended Interfacial Stability through Simple Acid Rinsing in a Li-Rich Oxide Cathode Material. *J. Am. Chem. Soc.* **2020**, *142*, 8522–8531. [[CrossRef](#)]
19. Fan, J.; Li, G.; Luo, D.; Fu, C.; Li, Q.; Zheng, J.; Li, L. Hydrothermal-Assisted Synthesis of Li-Rich Layered Oxide Microspheres with High Capacity and Superior Rate-capability as a Cathode for Lithium-ion Batteries. *Electrochim. Acta* **2015**, *173*, 7–16. [[CrossRef](#)]
20. Ji, X.; Xu, Y.; Xia, Q.; Zhou, Y.; Song, J.; Feng, H.; Wang, P.; Yang, J.; Tan, Q. Li-Deficient Materials-Decoration Restrains Oxygen Evolution Achieving Excellent Cycling Stability of Li-Rich Mn-Based Cathode. *ACS Appl. Mater. Interfaces* **2022**, *14*, 30133–30143. [[CrossRef](#)]
21. Cao, X.; Sun, J.; Chang, Z.; Wang, P.; Yue, X.; Okagaki, J.; He, P.; Yoo, E.; Zhou, H. Enabling Long-Term Cycling Stability within Layered Li-Rich Cathode Materials by O<sub>2</sub>/O<sub>3</sub>-Type Biphasic Design Strategy. *Adv. Funct. Mater.* **2022**, *32*, 2205199. [[CrossRef](#)]
22. Ates, M.N.; Jia, Q.; Shah, A.; Busnaina, A.; Mukerjee, S.; Abraham, K.M. Mitigation of Layered to Spinel Conversion of a Li-Rich Layered Metal Oxide Cathode Material for Li-Ion Batteries. *J. Electrochem. Soc.* **2014**, *161*, A290–A301. [[CrossRef](#)]
23. Chen, G.; An, J.; Meng, Y.; Yuan, C.; Matthews, B.; Dou, F.; Shi, L.; Zhou, Y.; Song, P.; Wu, G.; et al. Cation and anion Co-doping synergy to improve structural stability of Li- and Mn-rich layered cathode materials for lithium-ion batteries. *Nano Energy* **2019**, *57*, 157–165. [[CrossRef](#)]
24. Li, L.; Song, B.H.; Chang, Y.L.; Xia, H.; Yang, J.R.; Lee, K.S.; Lu, L. Retarded phase transition by fluorine doping in Li-rich layered Li<sub>1.2</sub>Mn<sub>0.54</sub>Ni<sub>0.13</sub>Co<sub>0.13</sub>O<sub>2</sub> cathode material. *J. Power Sources* **2015**, *283*, 162–170. [[CrossRef](#)]
25. Qiu, Y.; Peng, X.; Zhou, L.; Song, Y.; Bi, L.; Long, X.; He, L.; Xie, Q.; Wang, S.; Liao, J. Building Ultrathin Li<sub>4</sub>Mn<sub>5</sub>O<sub>12</sub> Shell for Enhancing the Stability of Cobalt-Free Lithium-Rich Manganese Cathode Materials. *Batteries* **2023**, *9*, 123. [[CrossRef](#)]
26. Zhang, J.; Zhang, D.; Wang, Z.; Zheng, F.; Zhong, R.; Hong, R. AlF<sub>3</sub> coating improves cycle and voltage decay of Li-rich manganese oxides. *J. Mater. Sci.* **2023**, *58*, 4525–4540. [[CrossRef](#)]
27. Dong, S.; Zhou, Y.; Hai, C.; Zeng, J.; Sun, Y.; Ma, Y.; Shen, Y.; Li, X.; Ren, X.; Sun, C.; et al. Enhanced Cathode Performance: Mixed Al<sub>2</sub>O<sub>3</sub> and LiAlO<sub>2</sub> Coating of Li<sub>1.2</sub>Ni<sub>0.13</sub>Co<sub>0.13</sub>Mn<sub>0.54</sub>O<sub>2</sub>. *ACS Appl. Mater. Interfaces* **2020**, *12*, 38153–38162. [[CrossRef](#)]
28. Zhao, Y.; Sun, Y.; Yue, Y.; Hu, X.; Xia, M. Carbon Modified Li-rich Cathode Materials Li<sub>1.26</sub>Fe<sub>0.22</sub>Mn<sub>0.52</sub>O<sub>2</sub> Synthesized via Molten Salt Method with Excellent Rate Ability for Li-ion Batteries. *Electrochim. Acta* **2014**, *130*, 66–75. [[CrossRef](#)]
29. Hou, M.; Liu, J.; Guo, S.; Yang, J.; Wang, C.; Xia, Y. Enhanced electrochemical performance of Li-rich layered cathode materials by surface modification with P<sub>2</sub>O<sub>5</sub>. *Electrochem. Commun.* **2014**, *49*, 83–87. [[CrossRef](#)]
30. Shobana, M.K. Metal oxide coated cathode materials for Li ion batteries—A review. *J. Alloys Compd.* **2019**, *802*, 477–487. [[CrossRef](#)]

31. Seu, C.S.; Davis, V.K.; Pasalic, J.; Bugga, R.V. Aluminum Borate Coating on High-Voltage Cathodes for Li-Ion Batteries. *J. Electrochem. Soc.* **2015**, *162*, A2259–A2265. [[CrossRef](#)]
32. Zheng, J.; Gu, M.; Xiao, J.; Polzin, B.J.; Yan, P.; Chen, X.; Wang, C.; Zhang, J. Functioning Mechanism of  $\text{AlF}_3$  Coating on the Li- and Mn-Rich Cathode Materials. *Chem. Mater.* **2014**, *26*, 6320–6327. [[CrossRef](#)]
33. Moghadam, Y.S.; Kharbachi, A.E.; Cambaz, M.A.; Dinda, S.; Diemant, T.; Hu, Y.; Melinte, G.; Fichtner, M. Borate-Based Surface Coating of Li-Rich Mn-Based Disordered Rocksalt Cathode Materials. *Adv. Mater. Interfaces* **2022**, *9*, 2201200. [[CrossRef](#)]
34. Kehoe, A.B.; Scanlon, D.O.; Watson, G.W. Role of lattice distortions in the oxygen storage capacity of divalently doped  $\text{CeO}_2$ . *Chem. Mater.* **2011**, *23*, 4464–4468. [[CrossRef](#)]
35. Jaksic, J.M.; Nan, F.; Papakonstantinou, G.D.; Botton, G.A.; Jaksic, M.M. Theory Substantiation and Properties of Novel Reversible Electrocatalysts for Oxygen Electrode Reactions. *J. Phys. Chem. C* **2015**, *119*, 11267–11285. [[CrossRef](#)]
36. Suzuki, T.; Kosacki, I.; Anderson, H.U. Electrical Conductivity and Lattice Defects in Nanocrystalline Cerium Oxide Thin Films. *J. Am. Ceram. Soc.* **2001**, *84*, 2007–2014. [[CrossRef](#)]
37. Tuller, H.L. Ionic conduction in nanocrystalline materials. *Solid State Ion.* **2000**, *131*, 143–157. [[CrossRef](#)]
38. Uberuaga, B.P.; Sickafus, K.E. Interpreting oxygen vacancy migration mechanisms in oxides using the layered structure motif. *Comput. Mater. Sci.* **2015**, *103*, 216–223. [[CrossRef](#)]
39. Deshpande, S.; Patil, S.; Kuchibhatla, S.V.; Seal, S. Size dependency variation in lattice parameter and valency states in nanocrystalline cerium oxide. *Appl. Phys. Lett.* **2005**, *87*, 133113. [[CrossRef](#)]
40. Lavik, E.B.; Kosacki, I.; Tuller, H.L.; Chiang, Y.M.; Ying, J.Y. Nonstoichiometry and electrical conductivity of nanocrystalline  $\text{CeO}_{2-x}$ . *J. Electroceram.* **1997**, *1*, 7–14. [[CrossRef](#)]
41. Ko, H.; Yang, G.; Wang, M.; Zhao, X. Isothermal crystallization kinetics and effect of crystallinity on the optical properties of nanosized  $\text{CeO}_2$  powder. *Ceram. Int.* **2014**, *40*, 6663–6671. [[CrossRef](#)]
42. Sreekanth, T.V.M.; Dillip, G.R.; Lee, Y.R. Picrasma quassioides mediated cerium oxide nanostructures and their post-annealing treatment on the microstructural, morphological and enhanced catalytic performance. *Ceram. Int.* **2016**, *42*, 6610–6618. [[CrossRef](#)]
43. Ha, H.; Yun, N.J.; Kim, M.H.; Woo, M.H.; Kim, K. Enhanced electrochemical and thermal stability of surface-modified  $\text{LiCoO}_2$  cathode by  $\text{CeO}_2$  coating. *Electrochim. Acta* **2006**, *51*, 3297–3302. [[CrossRef](#)]
44. Yao, J.; Wu, F.; Qiu, X.; Li, N.; Su, Y. Effect of  $\text{CeO}_2$ -coating on the electrochemical performances of  $\text{LiFePO}_4/\text{C}$  cathode material. *Electrochim. Acta* **2011**, *56*, 5587–5592. [[CrossRef](#)]
45. Ha, H.; Yun, N.J.; Kim, K. Improvement of electrochemical stability of  $\text{LiMn}_2\text{O}_4$  by  $\text{CeO}_2$  coating for lithium-ion batteries. *Electrochim. Acta* **2007**, *52*, 3236–3241. [[CrossRef](#)]
46. Ha, H.; Jeong, K.H.; Yun, N.J.; Hong, M.Z.; Kim, K. Effects of surface modification on the cycling stability of  $\text{LiNi}_{0.8}\text{Co}_{0.2}\text{O}_2$  electrodes by  $\text{CeO}_2$  coating. *Electrochim. Acta* **2005**, *50*, 3764–3769. [[CrossRef](#)]
47. Yuan, W.; Zhang, H.Z.; Liu, Q.; Li, G.R.; Gao, X.P. Surface modification of  $\text{Li}(\text{Li}_{0.17}\text{Ni}_{0.2}\text{Co}_{0.05}\text{Mn}_{0.58})\text{O}_2$  with  $\text{CeO}_2$  as cathode material for Li-ion batteries. *Electrochim. Acta* **2014**, *135*, 199–207. [[CrossRef](#)]
48. Zhou, M.; Zhao, J.; Qiu, S.; Tian, F.; Potapenko, O.; Zhong, S.; Potapenko, H.; Liang, Z. Structural and Electrochemical Properties of  $\text{Li}_{1.2}\text{Ni}_{0.16}\text{Mn}_{0.54}\text{Co}_{0.08}\text{O}_2\text{-Al}_2\text{O}_3$  Composite Prepared by Atomic Layer Deposition as the Cathode Material for LIBs. *Int. J. Electrochem. Sci.* **2020**, *15*, 10759–10771. [[CrossRef](#)]
49. Han, W.Q.; Wu, L.; Zhu, Y. Formation and Oxidation State of  $\text{CeO}_{2-x}$  Nanotubes. *J. Am. Chem. Soc.* **2005**, *127*, 12814–12815. [[CrossRef](#)]
50. Zhang, Y.; Wang, Z.B.; Yu, F.D.; Que, L.F.; Wang, M.J.; Xia, Y.F.; Xue, Y.; Wu, J. Studies on stability and capacity for long-life cycle performance of  $\text{Li}(\text{Ni}_{0.5}\text{Co}_{0.2}\text{Mn}_{0.3})\text{O}_2$  by Mo modification for lithium-ion battery. *J. Power Sources* **2017**, *358*, 1–12. [[CrossRef](#)]
51. Johnson, C.S.; Li, N.; Lefief, C.; Thackeray, M.M. Anomalous capacity and cycling stability of  $x\text{Li}_2\text{MnO}_3 \cdot (1-x)\text{LiMO}_2$  electrodes ( $\text{M} = \text{Mn, Ni, Co}$ ) in lithium batteries at 50 °C. *Electrochem. Commun.* **2007**, *9*, 787–795. [[CrossRef](#)]
52. Chen, Y.; Chen, Z.; Xie, K. Effect of annealing on the first-cycle performance and reversible capabilities of lithium-rich layered oxide cathodes. *J. Phys. Chem. C* **2014**, *118*, 11505–11511. [[CrossRef](#)]
53. Liu, J.; Wu, Z.; Yu, M.; Hu, H.; Zhang, Y.; Zhang, K.; Du, Z.; Cheng, F.; Chen, J. Building Homogenous  $\text{Li}_2\text{TiO}_3$  Coating Layer on Primary Particles to Stabilize Li-Rich Mn-Based Cathode Materials. *Small* **2022**, *18*, 2106337. [[CrossRef](#)]
54. Kang, S.H.; Kempgens, P.; Greenbaum, S.; Kropf, A.J.; Aminea, K.; Thackeraya, M.M. Interpreting the structural and electrochemical complexity of  $0.5\text{Li}_2\text{MnO}_3\text{-}0.5\text{LiMO}_2$  electrodes for lithium batteries ( $\text{M} = \text{Mn}_{0.5-x}\text{Ni}_{0.5-x}\text{Co}_{2x}$ ,  $0 \leq x \leq 0.5$ ). *J. Mater. Chem.* **2007**, *17*, 2069–2077. [[CrossRef](#)]
55. Zheng, J.; Gu, M.; Genc, A.; Xiao, J.; Xu, P.; Chen, X.; Zhu, Z.; Zhao, W.; Pullan, L.; Wang, C.; et al. Mitigating voltage fade in cathode materials by improving the atomic level uniformity of elemental distribution. *Nano Lett.* **2014**, *14*, 2628–2635. [[CrossRef](#)] [[PubMed](#)]
56. Kalyani, P.; Chitra, S.; Mohan, T.; Gopukumar, S. Lithium metal rechargeable cells using  $\text{Li}_2\text{MnO}_3$  as the positive electrode. *J. Power Sources* **1999**, *80*, 103–106. [[CrossRef](#)]
57. Wang, X.; Zheng, X.; Liao, Y.; Huang, Q.; Xing, L.; Xu, M.; Li, W. Maintaining structural integrity of 4.5 V lithium cobalt oxide cathode with fumaronitrile as a novel electrolyte additive. *J. Power Sources* **2017**, *338*, 108–116. [[CrossRef](#)]
58. Li, J.; Xing, L.; Wang, Z.; Tu, W.; Yang, X.; Lin, Y.; Liao, Y.; Xu, M.; Li, W. Insight into the capacity fading of layered lithium-rich oxides and its suppression via a film-forming electrolyte additive. *RSC Adv.* **2018**, *8*, 25794–25801. [[CrossRef](#)]

59. Chen, J.; Gao, Y.; Li, C.; Zhang, H.; Liu, J.; Zhang, Q. Interface modification in high voltage spinel lithium-ion battery by using N-methylpyrrole as an electrolyte additive. *Electrochim. Acta* **2015**, *178*, 127–133. [[CrossRef](#)]
60. Li, J.; Zhang, L.; Yu, L.; Fan, W.; Wang, Z.; Yang, X.; Lin, Y.; Xing, L.; Xu, M.; Li, W. Understanding Interfacial Properties between Li-Rich Layered Oxide and Electrolyte Containing Triethyl Borate. *J. Phys. Chem. C* **2016**, *120*, 26899–26907. [[CrossRef](#)]
61. Xu, K. Nonaqueous Liquid Electrolytes for Lithium-Based Rechargeable Batteries. *Chem. Rev.* **2004**, *104*, 4303–4417. [[CrossRef](#)] [[PubMed](#)]
62. Song, B.; Day, S.J.; Sui, T.; Lu, L.; Tang, C.C.; Korsunsky, A.M. Mitigated phase transition during first cycle of a Li-rich layered cathode studied by in operando synchrotron X-ray powder diffraction. *Phys. Chem. Chem. Phys.* **2016**, *18*, 4745–4752. [[CrossRef](#)] [[PubMed](#)]
63. Zhang, X.D.; Shi, J.L.; Liang, J.Y.; Yin, Y.Y.; Zhang, J.Z.; Yu, X.Q.; Guo, Y.G. Suppressing Surface Lattice Oxygen Release of Li-Rich Cathode Materials via Heterostructured Spinel  $\text{Li}_4\text{Mn}_5\text{O}_{12}$  Coating. *Adv. Mater.* **2018**, *30*, 1801751. [[CrossRef](#)]
64. Choi, S.M.; Kang, I.S.; Sun, Y.K.; Song, J.H.; Chung, S.M.; Kim, D.W. Cycling characteristics of lithium metal batteries assembled with a surface modified lithium electrode. *J. Power Sources* **2013**, *244*, 363–368. [[CrossRef](#)]
65. Ruff, Z.; Xu, C.; Grey, C.P. Transition Metal Dissolution and Degradation in NMC811-Graphite Electrochemical Cells. *J. Electrochem. Soc.* **2021**, *168*, 060518. [[CrossRef](#)]
66. Li, W. An Unpredictable Hazard in Lithium-ion Batteries from Transition Metal Ions: Dissolution from Cathodes, Deposition on Anode and Elimination Strategies. *J. Electrochem. Soc.* **2020**, *167*, 090514. [[CrossRef](#)]
67. Li, B.; Wang, Y.; Rong, H.; Wang, Y.; Liu, J.; Xing, L.; Xu, M.; Li, W. A novel electrolyte with the ability to form a solid electrolyte interface on the anode and cathode of a  $\text{LiMn}_2\text{O}_4$ /graphite battery. *J. Mater. Chem. A* **2013**, *1*, 12954–12961. [[CrossRef](#)]
68. Verma, P.; Maire, P.; Novak, P. A review of the features and analyses of the solid electrolyte interphase in Li-ion batteries. *Electrochim. Acta* **2010**, *55*, 6332–6341. [[CrossRef](#)]
69. Dekoven, B.M.; Hagans, P.L. XPS studies of metal/polymer interfaces—Thin films of Al on polyacrylic acid and polyethylene. *Appl. Surf. Sci.* **1986**, *27*, 199–213. [[CrossRef](#)]
70. Lazarraga, M.G.; Pascual, L.; Gadjov, H.; Kovacheva, D.; Petrov, K.; Amarilla, J.M.; Rojas, R.M.; Luengo-Martin, M.A.; Rojo, J.M. Nanosize  $\text{LiNi}_y\text{Mn}_{2-y}\text{O}_4$  ( $0 < y \leq 0.5$ ) spinels synthesized by a sucrose-aided combustion method: Characterization and electrochemical performance. *J. Mater. Chem.* **2004**, *14*, 1640–1647.
71. Guo, K.; Qi, S.; Wang, H.; Huang, J.; Wu, M.; Yang, Y.; Li, X.; Ren, Y.; Ma, J. High-Voltage Electrolyte Chemistry for Lithium Batteries. *Small Sci.* **2022**, *2*, 2100107. [[CrossRef](#)]
72. Gao, H.; Maglia, F.; Lamp, P.; Amine, K.; Chen, Z. Mechanistic Study of Electrolyte Additives to Stabilize High-Voltage Cathode–Electrolyte Interface in Lithium-Ion Batteries. *ACS Appl. Mater. Interfaces* **2017**, *9*, 44542–44549. [[CrossRef](#)]
73. Li, B.; Wang, Y.; Lin, H.; Liu, J.; Xing, L.; Xu, M.; Li, W. Improving high voltage stability of lithium cobalt oxide/graphite battery via forming protective films simultaneously on anode and cathode by using electrolyte additive. *Electrochim. Acta* **2014**, *141*, 263–270. [[CrossRef](#)]
74. Liu, Y.; Wang, K.; Lin, Y.; Zhu, Y.; Tu, W.; Xu, M.; Liu, X.; Li, B.; Li, W. Tetrafluoroterephthalonitrile: A Novel Electrolyte Additive for High-Voltage Lithium Cobalt Oxide/Graphite Battery. *Electrochim. Acta* **2017**, *256*, 307–315. [[CrossRef](#)]

**Disclaimer/Publisher’s Note:** The statements, opinions and data contained in all publications are solely those of the individual author(s) and contributor(s) and not of MDPI and/or the editor(s). MDPI and/or the editor(s) disclaim responsibility for any injury to people or property resulting from any ideas, methods, instructions or products referred to in the content.